Supplementary Material: Ramsey Envelope Modulation in NV Diamond Magnetometry

Jner Tzern Oon,[1,2,*] Jiashen Tang,[1,2,*] Connor A. Hart,[2,3] Kevin S. Olsson,[2,3,4] Matthew J. Turner,[2,3] Jennifer M. Schloss,[5] and Ronald L. Walsworth[1,2,3]

[1] *Department of Physics, University of Maryland, College Park, Maryland 20742, USA*
[2] *Quantum Technology Center, University of Maryland, College Park, Maryland 20742, USA*
[3] *Department of Electrical Engineering and Computer Science, University of Maryland, College Park, Maryland 20742, USA*
[4] *Intelligence Community Postdoctoral Research Fellowship Program, University of Maryland, College Park, Maryland 20742, USA*
[5] *Lincoln Laboratory, Massachusetts Institute of Technology, Lexington, Massachusetts 02421, USA*

(Dated: August 1, 2022)

CONTENTS

I. Theoretical Details 1
II. Experimental Details 3
III. Bias Field Misalignment Angle 4
IV. Microwave Frequency Calibration 5
V. Measured Ramsey Time Series Fit Details 5
VI. Ramsey Measurements Across Misalignment Angles 6
VII. QuTiP Simulations 7
VIII. Normalized Inverse Sensitivity 8
IX. Transverse Hyperfine Parameter 9
X. Double-quantum Envelope Amplitude 9
References 10

I. THEORETICAL DETAILS

This section provides a detailed derivation of the expressions given in Sec. II of the main text. We start with the NV ground state Hamiltonian H, including the effects of a magnetic field restricted to the x-z plane and the hyperfine interaction between the NV electronic spin and the onsite nitrogen nuclear spin,

$$\frac{H}{\hbar} = DS_z^2 - \gamma_e \left(B_z\hat{S}_z + B_x\hat{S}_x\right) - \gamma_n g_n \left(B_z\hat{I}_z + B_x\hat{I}_x\right) + A_{||}\hat{S}_z\hat{I}_z + A_\perp \left(\hat{S}_x\hat{I}_x + \hat{S}_y\hat{I}_y\right). \tag{S1}$$

The contributions to H_0 can be separated into secular and non-secular contributions H_S and H_{NS}, respectively. The secular term H_S consists of contributions that commute with operator $\hat{S}_z$. Conversely, the non-secular terms H_{NS} do not commute with $\hat{S}_z$ and are capable of driving transitions within the electronic spin system. This is summarized as

* These authors contributed equally to this work. jjoon@umd.edu

follows:

$$\begin{aligned} H &= H_S + H_{NS} \\ \frac{H_S}{\hbar} &\equiv D\hat{S}_z^2 - \gamma_e B_z \hat{S}_z - \gamma_n g_n \left(B_z \hat{I}_z + B_x \hat{I}_x \right) + A_{||} \hat{S}_z \hat{I}_z \\ \frac{H_{NS}}{\hbar} &\equiv -\gamma_e B_x \hat{S}_x + A_\perp \left(\hat{S}_x \hat{I}_x + \hat{S}_y \hat{I}_y \right). \end{aligned} \tag{S2}$$

We begin by reproducing work done by Childress *et al.* [1] and Myers [2]. The Hamiltonian is expanded as a series determined by order D, the largest energy scale within the Hamiltonian for the magnetic fields $B < 200\,\mathrm{G}$ used in our study. The non-secular terms H_{NS} are treated as a perturbation to the secular Hamiltonian H_S. Using second order perturbation theory, we obtain the leading order correction to the Hamiltonian $H_{m_s}^{(1)}$ for a given electron spin quantum number m_s,

$$\hat{P}_{m_s} H_S + H_{m_s}^{(1)} = \hat{P}_{m_s} H_{NS} \frac{1}{E_{m_s} - \left(\mathbb{1} - \hat{P}_{m_s} \right) H_S \left(\mathbb{1} - \hat{P}_{m_s} \right)} H_{NS} \hat{P}_{m_s}, \tag{S3}$$

with projection operator $\hat{P}_{m_s} \equiv |m_s\rangle \langle m_s|$ and identity operator $\mathbb{1}$. An effective nuclear g-tensor $g_n(m_s)$ is defined by evaluating the change in the Hamiltonian with respect to the magnetic field,

$$\begin{aligned} g_n(m_s) &= \frac{d}{dB} \left(\hat{P}_{m_s} H_S + H_{m_s}^{(1)} \right) \\ &= \begin{pmatrix} 1 & 0 & 0 \\ 0 & 1 & 0 \\ 0 & 0 & 1 \end{pmatrix} - \frac{\gamma_e}{\gamma_n D} (2 - 3|m_s|) \begin{pmatrix} A_\perp & 0 & 0 \\ 0 & A_\perp & 0 \\ 0 & 0 & 0 \end{pmatrix}. \end{aligned} \tag{S4}$$

This effective nuclear g-tensor is substituted into the expression for H_S. After introducing an enhancement parameter $\kappa = \frac{\gamma_e A_\perp}{\gamma_n D} \approx 8.26$, the following Hamiltonian is obtained:

$$\begin{aligned} H_1 =& D\hat{S}_z^2 - \gamma_e B_z \hat{S}_z + A_{||} \hat{S}_z \hat{I}_z - 3\kappa \gamma_n B_x \hat{S}_z^2 \hat{I}_x \\ & - \gamma_n \left(B_z \hat{I}_z + (1 - 2\kappa) B_x \hat{I}_x \right). \end{aligned} \tag{S5}$$

After moving into an electronic doubly-rotating frame [3] using the unitary transformation

$$\begin{aligned} R_1(t) &\equiv \left(e^{i\lambda_1 t} |m_s = +1\rangle \langle m_s = +1| + |m_s = 0\rangle \langle m_s = 0| + e^{i\lambda_2 t} |m_s = -1\rangle \langle m_s = -1| \right) \otimes \mathbb{1}_n \\ &= \begin{pmatrix} e^{i\lambda_1 t} & 0 & 0 \\ 0 & 1 & 0 \\ 0 & 0 & e^{i\lambda_2 t} \end{pmatrix} \otimes \begin{pmatrix} 1 & 0 \\ 0 & 1 \end{pmatrix} \end{aligned}, \tag{S6}$$

with $\lambda_{1,2} = D \mp \gamma_e B_z$, we obtain the Hamiltonian $\widetilde{H}_1$ given in Eq. (S7), which is also given in the main text as Eq. (2). Experimentally this Hamiltonian is realized using microwave fields to probe transitions $|m_s = 0\rangle \leftrightarrow |m_s = +1\rangle$ and/or $|m_s = 0\rangle \leftrightarrow |m_s = -1\rangle$, equally detuned from the two hyperfine resonances.

$$\begin{aligned} \widetilde{H}_1 &= R_1(t) H_1 R_1(t)^\dagger + i \frac{dR_1(t)}{dt} R_1(t)^\dagger \\ &= \underbrace{A_{||} \hat{S}_z \hat{I}_z - 3\kappa \gamma_n B_x \hat{S}_z^2 \hat{I}_x}_{\text{depends on } m_s} - \underbrace{\gamma_n \left(B_z \hat{I}_z + (1 - 2\kappa) B_x \hat{I}_x \right)}_{\text{independent of } m_s} \end{aligned} \tag{S7}$$

An additional rotation using $R_2(t) = e^{i\phi \hat{I}_y}$ further simplifies the Hamiltonian, with $\phi = \tan^{-1}\left(\frac{(1-2\kappa)B_x}{B_z} \right)$. This rotation diagonalizes the nuclear subsystem that is independent of the electron spin, producing the following Hamiltonian:

$$\begin{aligned} \widetilde{H}_2 &= R_2(t) \widetilde{H}_1 R_2(t)^\dagger + i \frac{dR_2(t)}{dt} R_2(t)^\dagger \\ &= -\gamma_n \left(\vec{\beta}_{\text{ind}} + \vec{\beta}(m_s) \right) \cdot \vec{I}. \end{aligned} \tag{S8}$$

Equation (S8), also provided in the main text as Eq. (3), consists of an effective magnetic field $\vec{\beta}_{\text{ind}} + \vec{\beta}(m_s)$ interacting with the nuclear spin. This vector sum consists of:

1. a magnetic field along the newly defined z'-axis, *independent* of the electronic spin state,

$$\vec{\beta}_{\text{ind}} = \beta_{\text{ind}}\hat{z'} = \sqrt{B_z^2 + (1-2\kappa)^2 B_x^2}\,\hat{z'}, \tag{S9}$$

2. and a spin-*dependent* field

$$\vec{\beta}(m_s) = \begin{bmatrix}\beta_{x'}(m_s)\\ \beta_{y'}(m_s)\\ \beta_{z'}(m_s)\end{bmatrix} = \frac{1}{\beta_{\text{ind}}}\begin{bmatrix} B_x\left(m_s(1-2\kappa)\frac{A_{||}}{\gamma_n} + m_s^2 3\kappa B_z\right)\\ 0\\ -m_s\frac{A_{||}}{\gamma_n}B_z + m_s^2 3\kappa(1-2\kappa)B_x^2\end{bmatrix}. \tag{S10}$$

An additional rotation generated by $\hat{I}_{y'}$ by an angle ϕ_{m_s} diagonalizes the Hamiltonian, depending on the electronic spin state m_s,

$$\phi_{m_s} = \tan^{-1}\left(\frac{\beta_{x'}(m_s)}{\beta_{\text{ind}} + \beta_{z'}(m_s)}\right). \tag{S11}$$

From Eq. (S8), the effective nuclear Larmor precession frequency can be obtained,

$$\begin{aligned}\omega_{m_s} = \left|\gamma_n\left(\vec{\beta}_{\text{ind}} + \vec{\beta}(m_s)\right)\right| &= -\gamma_n\sqrt{\left(\beta_{\text{ind}} + \beta_{z'}(m_s)\right)^2 + \beta_{x'}(m_s)^2}\\ &= -\gamma_n\sqrt{B_x^2\left(1-2\kappa+m_s^2 3\kappa\right)^2 + \left(m_s\frac{A_{||}}{\gamma_n} - B_z\right)^2}.\end{aligned} \tag{S12}$$

For a given electronic spin state m_s, the nuclear spin precesses at a corresponding frequency ω_{m_s}. Note that when $m_s = 0$, this reduces to the spin-independent Larmor frequency $\omega_0 = |\gamma_n\beta_{\text{ind}}|$.

For a single-quantum (SQ) Ramsey sequence, we effectively operate within a 2-level system consisting of $|m_s = 0\rangle$ and either $|m_s = +1\rangle$ or $|m_s = -1\rangle$. To apply a microwave rotation pulse, we define the unitary operator $\hat{U}_x(\theta) = e^{-i\hat{\sigma}_x\theta/2}$ using the 2-level Pauli spin operator $\hat{\sigma}_x$. The SQ Ramsey sequence consists of two $\pi/2$ pulses separated by a free precession period of duration τ. The initial state $|\psi(0)\rangle = |m_s = 0\rangle$ evolves under the following unitary rotations:

$$\psi_{SQ}(t) = \hat{U}_x(\pi/2)\left(e^{-i\tilde{H}_2\tau/\hbar}\right)\hat{U}_x(\pi/2)\,|\psi(0)\rangle\,. \tag{S13}$$

The Ramsey response S_{SQ} can be represented by a projection $P_0 = |m_s = 0\rangle\langle m_s = 0|$ onto the $m_s = 0$ state,

$$\begin{aligned}S_{SQ}(\tau) &= \text{Tr}\left\{P_0\,|\psi_{SQ}(\tau)\rangle\langle\psi_{SQ}(\tau)|\right\}\\ &= \frac{1}{2}\left(1 - \cos\left(\frac{\omega_0\tau}{2}\right)\cos\left(\frac{\omega_{\pm1}\tau}{2}\right) + \cos\left(\Phi_{0,\pm1}\right)\sin\left(\frac{\omega_0\tau}{2}\right)\sin\left(\frac{\omega_{\pm1}\tau}{2}\right)\right).\end{aligned} \tag{S14}$$

This response represents the electronic spin population and therefore spans between 0 and 1. For tidiness, this form is slightly modified to give the expression in the main text $S_{i,j}(\tau) = 2S(\tau) - 1$, where $S(\tau)$ denotes the response shown in Eq. (S14). The double-quantum (DQ) response can be similarly obtained by substituting the 2-level spin operator σ_x in the unitary rotation $\hat{U}(\theta)$ with the appropriate spin-1 operator:

$$S_{DQ} = \frac{1}{2}\left[1 + \cos\left(\frac{\omega_{-1}\tau}{2}\right)\cos\left(\frac{\omega_{+1}\tau}{2}\right) - \cos\left(\Phi_{-1,+1}\right)\sin\left(\frac{\omega_{-1}\tau}{2}\right)\sin\left(\frac{\omega_{+1}\tau}{2}\right)\right] \tag{S15}$$

II. EXPERIMENTAL DETAILS

A diode-pumped solid-state laser (Lighthouse Photonics, Sprout-D5W) is employed to generate the continuous-wave 532 nm laser beam. The laser beam is passed through an acousto-optic modulator (AOM) (Gooch & Housego, Model: 3250-220) and the first order diffracted beam is used for the experiments. To create optical pulses for NV ensemble initialization and readout, the RF driver for the AOM is gated by switches (Mini-Circuits, ZASWA-2-50DR+) using transistor-transistor logic (TTL) pulses (Swabian Instruments, Pulse Streamer 8/2). The beam is focused through a $20\times/0.75$ NA Nikon objective onto the diamond, illuminating the NV-enriched layer over a spot of $\sim 20\,\mu$m diameter. The illumination intensity is kept below $0.1\,\text{mW}/\mu\text{m}^2$. The outgoing spin-dependent NV fluorescence is collected

through the same objective, passed through a 150 µm pinhole (Thorlabs, P150D) to restrict the collection volume, filtered by a 647 nm long pass filter (Semrock) and finally projected onto an avalanche photodiode (Hamamatsu C10508-01). Photodiode voltage measurements are acquired using a DAQ system (National Instruments, NI USB-6363). The bias magnetic field is generated using two permanent samarium cobalt (SmCo) ring magnets to minimize temperature sensitivity of the bias field. Rotation of the magnet pair for different misalignment angles is controlled using two sets of Thorlabs HDR50 rotation stages with stepper motors. Microwave fields are synthesized from up to two signal generators with built-in IQ mixers (Stanford Research System, SG384); and gated by switches and TTLs to provide either single- or double- quantum pulsed control of the NV ensemble spin states. The Ω-shaped planar waveguide for microwave delivery has a diameter ≈ 150 µm to ensure field homogeneity over the laser illumination area.

III. BIAS FIELD MISALIGNMENT ANGLE

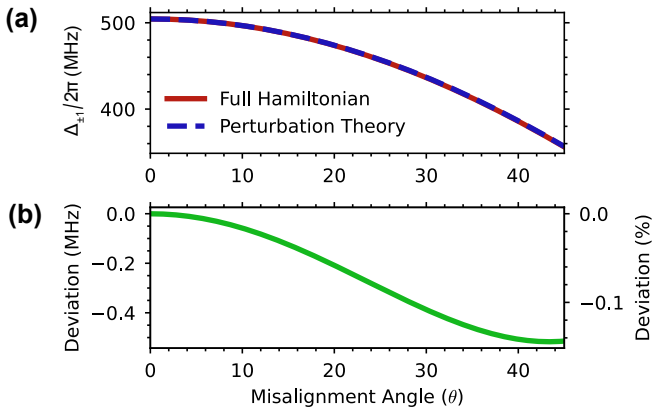


FIG. S1. Transition frequency difference $\Delta_{\pm1}$ between $m_s = 0 \leftrightarrow +1$ and $m_s = 0 \leftrightarrow -1$ resonances as a function of misalignment angle. Calculation is performed at 90 G. (a) Numerical results of $\Delta_{\pm1}$ using the full NV ground state Hamiltonian (solid red line) and the approximate formula from perturbation theory $2\gamma_e B\cos\theta$ (dashed blue line). (b) Absolute and percentage deviation of $\Delta_{\pm1}$ between the two calculation methods.

When the bias magnetic field is misaligned from the NV axis, both the transverse B_x and longitudinal B_z field components affect the energy levels of $|0\rangle, |\pm1\rangle$. In the main text, the resonance frequency difference $\Delta_{\pm1}$ between the two transitions $|m_s = 0\rangle \leftrightarrow |m_s = +1\rangle$ and $|m_s = 0\rangle \leftrightarrow |m_s = -1\rangle$ is used to calculate the misalignment angle θ, via the relationship $\Delta_{\pm1} \approx 2\gamma_e B_z = 2\gamma_e B\cos\theta$. This approximate relationship is obtained from time-independent perturbation theory. For the small bias field magnitudes $B \lesssim 110$ G used in our study, the large NV zero field splitting $D = 2\pi \times 2870$ MHz dominates the energy scale, $D \gg |\gamma_e B|$. This allows us to treat the transverse field B_x contribution as a perturbation, resulting in the eigenenergies $E_{|0\rangle\rightarrow|\pm1\rangle}$ accurate to the second order correction [4]:

$$\frac{E_{|0\rangle\rightarrow|\pm1\rangle}}{\hbar} = D + \frac{3\left|\gamma_e B_x\right|^2}{D} \pm \gamma_e B_z. \tag{S16}$$

Therefore, $\Delta_{\pm1} = \left(E_{|0\rangle\rightarrow|+1\rangle} - E_{|0\rangle\rightarrow|-1\rangle}\right)/\hbar$ can be accurately modeled by $2\gamma_e B\cos\theta$, up to second order. Using this relationship, the measurements of $\Delta_{\pm1}$ are converted to values of the misalignment angle θ. The error bars for θ in Fig. 3 of the main text indicate the corresponding 95% confidence interval (CI), except for cases where the standard deviation σ_θ calculated from error propagation is less than the stage rotation error. In these cases, the nominal accuracy ($\pm0.047°$) of the stage is used for σ_θ instead.

To verify that the expression for $\Delta_{\pm1}$ is indeed valid, we compare the measured values of $\Delta_{\pm1}$ to those obtained by diagonalizing the complete Hamiltonian given in Eq. (1). An example plot is shown in Fig. S1, for a 90 G bias field magnitude and misalignment angles θ up to 45°. We observe excellent agreement with the results obtained using the full Hamiltonian, with percentage deviation in $\Delta_{\pm1}$ of under 0.15%. The corresponding error contribution to the angle estimation is less than the dominant error values used for Fig. 3 in the main text.

IV. MICROWAVE FREQUENCY CALIBRATION

To set the microwave frequency to the center of the two ^{15}NV hyperfine-split transitions, we perform a two-step calibration procedure combining pulsed-ODMR and Ramsey techniques. First, the two hyperfine transitions are resolved by performing a pulsed-ODMR experiment with low microwave power (π pulse time ~ 900 ns). The resulting spectrum is fit to a sum of two Lorentzians $A - \sum_{i=1}^{2} \frac{C_i}{\pi} \frac{\frac{1}{2}\Gamma_i}{(\nu-\nu_i)^2+(\frac{1}{2}\Gamma_i)^2}$, with free parameters including the contrast C_i, line width Γ_i, frequency ν_i and overall offset A.

The mean of the two Lorentzian center frequencies $\nu_* = (\nu_1 + \nu_2)/2$ is used as the initial value of the applied microwave frequency. Next, a series of Ramsey $\pi/2 - \tau - \pi/2$ experiments are performed to refine this estimate. Fixing τ at a point of maximum contrast, the microwave frequency is varied around ν_* to produce an oscillating magnetometry curve [5]. Choosing a common phase for both microwave $\pi/2$ pulses, the extremum nearest to ν_* is used as the updated center resonance frequency. This calibrated value ν_*^{calib} is obtained by fitting the magnetometry curve to a sinusoidal function and extracting the necessary frequency offset.

V. MEASURED RAMSEY TIME SERIES FIT DETAILS

For fits to Ramsey time series data, we use a modified form of Eq. (6) from the main text:

$$\begin{aligned}&\widetilde{S}_{0,+1}(\tau)\\&= C_0 e^{-(\tau/T_2^*)^p}\left[-\cos\left(\frac{\omega_0}{2}\tau + x_0\right)\cos\left(\frac{\omega_{+1}}{2}\tau + x_{+1}\right) + \cos\left(\Phi_{0,+1}\right)\sin\left(\frac{\omega_0}{2}\tau + x_0\right)\sin\left(\frac{\omega_{+1}}{2}\tau + x_{+1}\right)\right] + B.\end{aligned} \tag{S17}$$

Here, τ represents the free evolution time in a Ramsey sequence. The free fit parameters are the initial contrast C_0, dephasing time T_2^*, stretched exponential factor p, EREEM frequency components ω_0 and ω_{+1}, amplitude modulation factor determined by $\Phi_{0,+1}$, phase offsets x_0 and x_{+1}, and a vertical offset B.

For each estimate of ω_0 or $\chi_{\min} = \cos(\Phi_{0,+1})$ reported in Fig. 3(b,c) of the main text, its corresponding confidence interval (CI) is constructed using the standard interval method. For each parameter estimate $\hat{\theta}$, its error bar represents a range bounded between $\hat{\theta} \pm z^{(0.95)}\hat{\sigma}$, where $\hat{\theta}$ represents the point estimate of the parameter of interest with standard error $\hat{\sigma}$, and $z^{(0.95)}$ denotes the 95^{th} percentile of the normal deviate. Both $\hat{\theta}$ and $\hat{\sigma}$ are calculated using maximum likelihood estimation via the MATLAB `lsqcurvefit` function. However, the exact CI can differ from the standard interval approximation if the measurement error is not normally distributed. In such scenarios, a bootstrap confidence interval produces a more accurate CI estimation [6]. To test this approach, we applied a bootstrap sampling method to four randomly selected data points from Fig. 3(b,c) in the main text. The distribution of fitted parameters resembles a normal distribution with $\sim 95\%$ data points located within $\hat{\theta} \pm z^{(0.95)}\hat{\sigma}$, which supports the reporting of CI estimates obtained by the standard interval method in the main text. A bootstrap fitting example for the envelope beat frequency ω_0 is shown in Fig. S2, for a bias field magnitude $B = 90.08(2)$ G and a misalignment angle $\theta = 25.72(9)^\circ$.

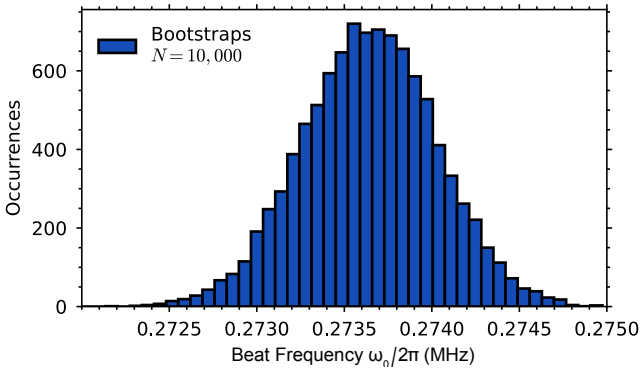


FIG. S2. Example bootstrap fit result for the EREEM beat frequency. Starting with a single Ramsey time series, 10,000 additional datasets are created by randomly sampling with replacement from the initial time series. Estimates of the EREEM beat frequency ω_0 are extracted using the MATLAB `lsqcurvefit` function for each dataset. The distribution supports the assumption of normality used by the standard interval method for confidence interval (CI) construction.

A fit to Eq. (S17) is appropriate when the microwave driving frequency is equally detuned from the two ^{15}NV

hyperfine-split transitions, $\left|\delta_{m_I=-\frac{1}{2}}\right| = \left|\delta_{m_I=\frac{1}{2}}\right|$. Alternatively, the EREEM beat frequency ω_0 can be extracted when these detunings are not equal $\left|\delta_{m_I=-\frac{1}{2}}\right| \neq \left|\delta_{m_I=\frac{1}{2}}\right|$. This approach comes at the expense of fitting accuracy due to the presence of extra frequency tones in the Ramsey signal. The Ramsey signal exhibits frequency splittings of magnitude ω_0 centered at both $\left|\delta_{m_I=-\frac{1}{2}}\right|$ and $\left|\delta_{m_I=\frac{1}{2}}\right|$, resulting in four distinct tones. To resolve all frequency components and to avoid ambiguity in the frequency assignments, the following condition is enforced: $\left|\delta_{m_I=-\frac{1}{2}}\right| - \left|\delta_{m_I=\frac{1}{2}}\right| \gg \omega_0$. This alternative measurement is conducted at four randomly selected field configurations, sampled from those shown in Fig. 3 of the main text. A four-tone EREEM function modified from Eq. (S17) is used for fits to the time series data. The extracted envelope beat frequencies overlap with the CI of the corresponding data at the same field configurations in the main text. Example data is shown in Fig. S3 for a bias field magnitude $B = 90.08(2)$ G and misalignment angle $\theta = 25.72(9)°$.

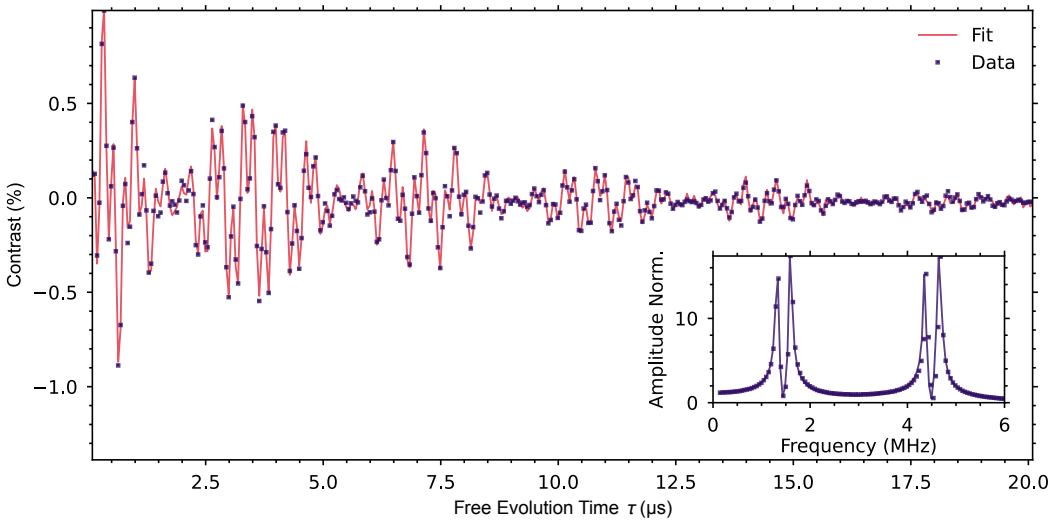


FIG. S3. Experimental Ramsey time series data obtained using a purposefully detuned microwave driving frequency, with its corresponding amplitude spectrum displayed as an inset. The larger detuning enables clear separation among all frequency components. The fit result for the EREEM beat frequency $\omega_0/2\pi$ is 273.3 ± 1.4 MHz, which overlaps with the confidence interval (CI) of the corresponding beat frequency fit result, 273.6 ± 0.8 kHz, obtained when the microwave frequency is centered between the hyperfine splitting.

VI. RAMSEY MEASUREMENTS ACROSS MISALIGNMENT ANGLES

Figure S4 shows experimental Ramsey time series data acquired at a range of bias field misalignment angles θ for a field magnitude of $B = 90.09(2)$ G, in both time and frequency domains. When the magnetic field is aligned to the NV axis ($\theta = 0$), the measured time series oscillate with a single frequency, represented by an individual peak in the amplitude spectrum. After introducing a misalignment, a beating (EREEM) is observed that results in a frequency splitting of magnitude ω_0, which increases as a function of θ. At each field configuration (B, θ), the time series measurements are fit to Eq. S17 to extract the envelope modulation properties. The results of these fits are shown in Fig. 3 of the main text, which includes measurements at magnetic field magnitudes $B = 50.49(2)$ G, $69.40(2)$ G, and $110.78(2)$ G.

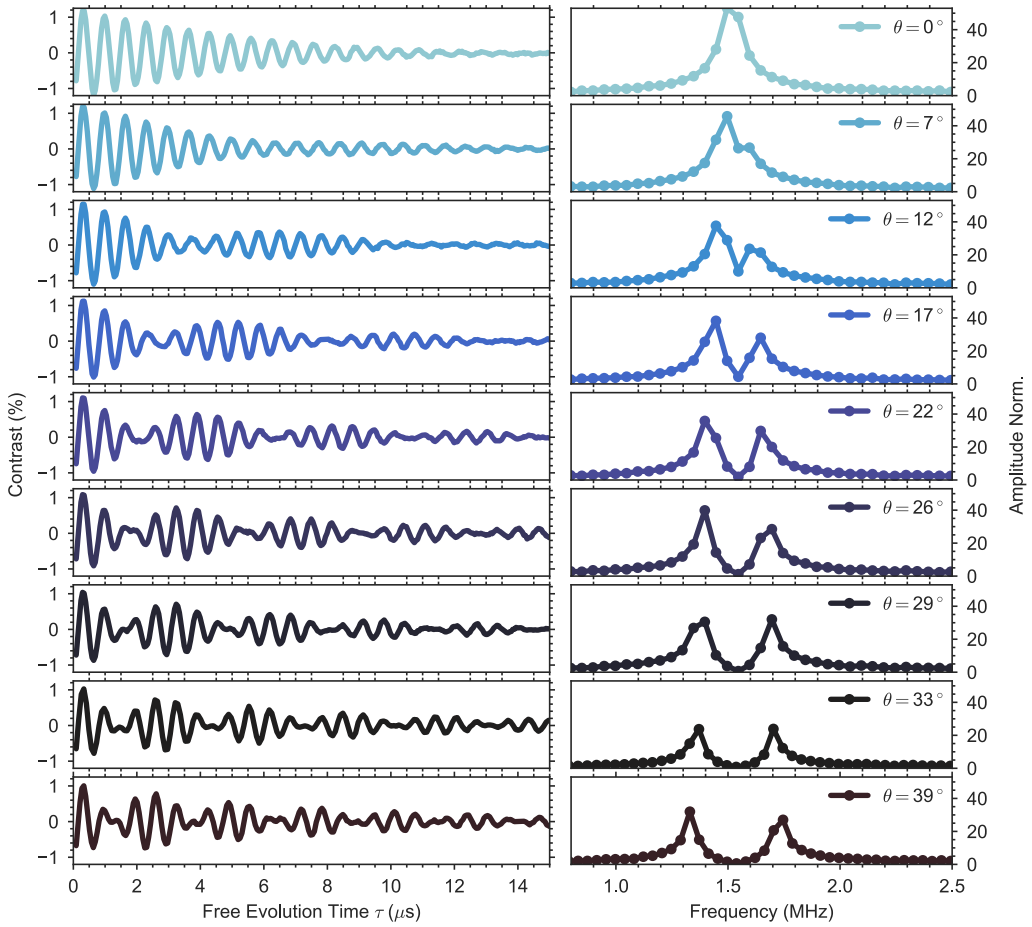


FIG. S4. Experimental single-quantum Ramsey time series measurements (left column) and corresponding amplitude spectra (right column) at various bias field misalignment angles θ, at a bias field magnitude of 90.08(2) G.

VII. QUTIP SIMULATIONS

As discussed in Sec. IV of the main text, systematic differences are observed between experimental estimates of the Ramsey envelope beat frequency ω_0, and theoretical predictions from Eq. (7) of the main text obtained using second order perturbation theory. This equation is reproduced below for clarity.

$$\begin{aligned}\omega_0 = |\gamma_n \beta_{\text{ind}}| &= |\gamma_n| \sqrt{B_z^2 + (1-2\kappa)^2 B_x^2} \\ &= |\gamma_n| \, B \sqrt{1 + 4(\kappa^2 - \kappa)\sin^2\theta}.\end{aligned} \tag{7}$$

The observed difference increases with the bias magnetic field misalignment angle. To study this discrepancy, we conduct numerical simulations of Ramsey spin dynamics for a range of bias field configurations, using the QuTiP package in Python. For a coupled NV electron-nuclear system initially described by the lab frame Hamiltonian in Eq. (1) of the main text, applied microwave pulses are modeled using time-dependent contributions $\Omega(t)\cos(\omega_e t + \varphi)\hat{S}_x$. The AC magnetic field amplitude $\Omega(t)$ is chosen to yield a 20 MHz Rabi frequency during pulses. The duration of each pulse is calibrated so a $\pi/2$ rotation is performed. The phase φ is used to toggle between pulse rotation axes.

To evaluate the state evolution during the Ramsey sequence, we employ the master equation solver function *mesolve* provided by the QuTiP module. To adjust the accuracy of the ordinary differential equation solver used for these calculations, absolute and relative tolerance values are supplied to the function, denoted by *atol* and *rtol*, respectively. These user-defined tolerance values are determined empirically by comparing the accuracy of the NV system dynamics after several Rabi cycles, with values $atol = rtol = 10^{-9}$ chosen for all Ramsey simulations. The system state is recorded at regular 10 ns time steps during the Ramsey free evolution interval, but the solver is allowed to perform up to 10^6 additional evaluations within each time step. Note that all timescales and frequencies are scaled by 6 orders of magnitude for simplicity of use (e.g., setting time = 1 represents 1 μs).

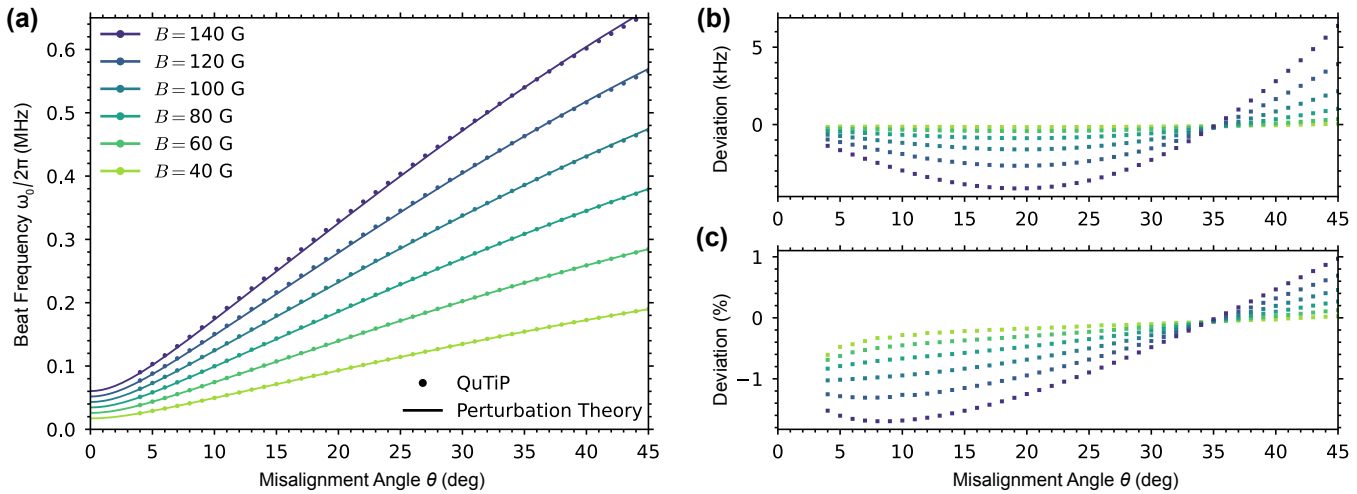


FIG. S5. Calculation and comparison of Ramsey envelope (EREEM) beat frequency ω_0 as a function of bias magnetic field magnitude and misalignment angle, using analytical approximation and QuTiP numerical simulations. (a) ω_0 obtained using numerical simulations (circles) and analytical perturbation theory (solid line), for magnetic fields between 40 G and 140 G. (b) Absolute differences between ω_0 estimates from QuTiP numerical simulations and analytical approximation, for the field configurations shown in (a). (c) Percentage deviation between ω_0 estimates from QuTiP numerical simulations and analytical approximation.

For each field configuration, the lab frame Hamiltonian H is first diagonalized to obtain eigenenergies and eigenstates. The pair of frequencies for transitions between $|m_s = 0, m_I = +1/2\rangle \leftrightarrow |1, +1/2\rangle$ and $|0, -1/2\rangle \leftrightarrow |1, -1/2\rangle$ are calculated. The mean of these two values is used as the frequency ω_e of the pulses. Starting with an initial state $|0, -1/2\rangle$, the Ramsey pulse sequence is applied and the final population in the $m_s = 0$ state is determined. Pulse sequences are simulated for a range of free evolution times τ, and the resulting time series is fit to Eq. (S14) to extract the parameters ω_0, $\omega_{\pm 1}$ and $\Phi_{0,\pm 1}$. In Fig. S5, the values of ω_0 extracted from numerical simulations are compared to the analytical predictions given by Eq. (7). For the field configurations considered in the main text, the difference between these calculations remains around or below 1%.

VIII. NORMALIZED INVERSE SENSITIVITY

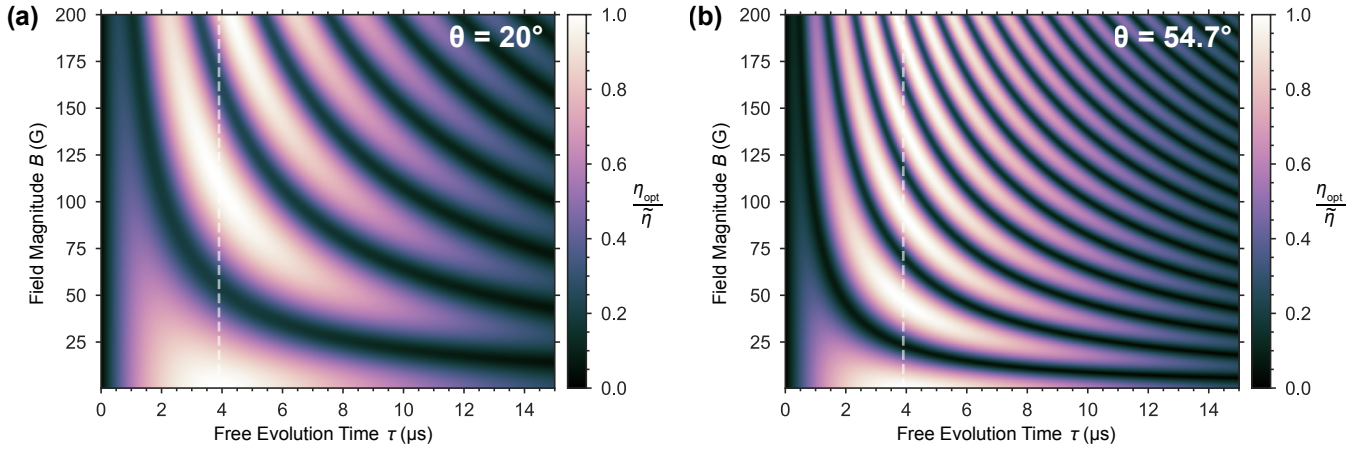


FIG. S6. 2D color plots of the normalized inverse sensitivity with respect to the Ramsey free evolution time τ and bias magnetic field magnitude B, at 2 distinct misalignment angles $\theta = 20°$ (a) and 54.7° (b)

In Fig. 4(c) of the main text, a 2D color plot of the relative normalized inverse magnetic field sensitivity is shown, evaluated using Eq. (9). These calculations are repeated here for two other misalignment angles $\theta = 20°, 54.7°$ and

are shown in Fig. S6. The experimental timescales assumed here ($T_D = 5\,\mu s$, $T_2^* = 5\mu s$) are the same as those used in the main text. In particular, the $\theta = 54.7°$ case can describe a bias magnetic field oriented to have equal projections onto all four NV quantization axes.

IX. TRANSVERSE HYPERFINE PARAMETER

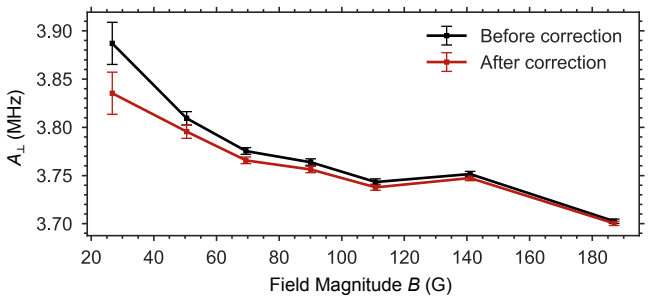


FIG. S7. Results for the transverse hyperfine parameter $A_\perp$ as a fit parameter to the Ramsey envelope (EREEM) beat frequency ω_0, extracted from experimental data, for a range of magnetic fields, with error bars showing the 95% confidence interval, shown in black. Estimated corrections to values of $A_\perp$ are depicted in red, using the discrepancy between QuTiP numerical simulations and theoretical predictions of ω_0.

As discussed in Sec. IV of the main text, we perform fits of Eq. (7) to experimental measurements of ω_0 while allowing the transverse hyperfine parameter $A_\perp$ to vary as a degree of freedom. We repeat this process at a series of bias field magnitudes, extending beyond those considered in the main text. The resulting fits for $A_\perp$ are shown in Fig. S7 using black markers, with error bars representing a 95% confidence interval (CI). We observe an overall decrease of $A_\perp$ as the field magnitude is increased.

Due to the field-dependent discrepancy of ω_0 between QuTiP simulations and the predictions of perturbation theory, additional corrections are necessary to precisely determine $A_\perp$. However, as shown in Fig. S5, the degree to which these predictions differ depends on the misalignment angle θ. As an initial attempt to estimate these corrections, we fit Eq. (7) to the estimates of ω_0 obtained using QuTiP simulations, at the specific magnetic field magnitudes and misalignment angles studied in experiment. The absolute difference between these fits and the originally assumed value for $A_\perp$ is used to update the experimentally determined $A_\perp$ estimates, shown in Fig. S7 as red points. We expect that future studies can further refine the estimation of $A_\perp$ by increasing the sampling of misalignment angles at each magnetic field magnitude. In addition, improvements to the electronic dephasing time T_2^* can enhance the measurement precision of ω_0 (and therefore $A_\perp$) at lower fields. For example, this may be achieved by optimizing the diamond sample or using techniques such as spin-bath driving [4]. Alternatively, an extension of these studies to higher bias field magnitudes will allow direct comparisons to the previously conducted EPR study [7].

X. DOUBLE-QUANTUM ENVELOPE AMPLITUDE

In Fig. 5(c) of the main text, 2D color plots of the relative contrast at amplitude modulation nodes $\chi_{\min}$ are shown for both single-quantum (SQ) and double-quantum (DQ) Ramsey. The calculations for DQ Ramsey are reproduced here, with the range of magnetic field magnitudes and misalignment angles extended up to 800 G and 90°, respectively. For the magnetic field magnitudes considered in this study $B \lesssim 200\,G$, the contrast at envelope modulation nodes is well-preserved ($\chi_{\min} \approx 1$). However, the calculations illustrated in Fig. S8 show that for a sufficiently large magnetic field, the DQ Ramsey signal can exhibit significant envelope modulations.

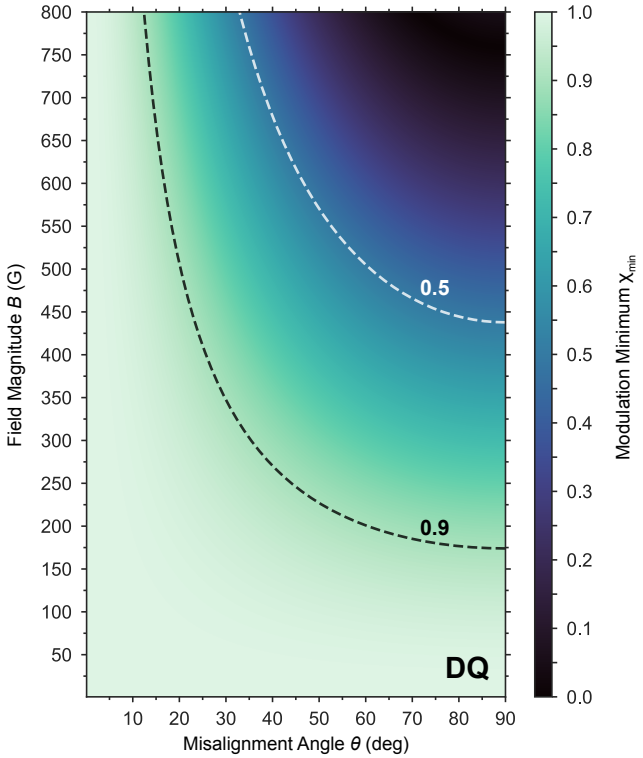


FIG. S8. Calculated double-quantum (DQ) Ramsey relative contrast at amplitude modulation nodes $\chi_{\min} = |\cos(\Phi_{-1,+1})|$, for magnetic field magnitudes B up to 800 G and misalignment angles up to 90°. Dashed contour lines indicate magnetic field configurations where $\chi_{\min}$ equals 0.9 and 0.5, representing 10% and 50% contrast loss at envelope nodes, respectively.

[1] L. Childress, M. V. G. Dutt, J. M. Taylor, A. S. Zibrov, F. Jelezko, J. Wrachtrup, P. R. Hemmer, and M. D. Lukin, Coherent dynamics of coupled electron and nuclear spin qubits in diamond, Science **314**, 281 (2006).

[2] B. Myers, *Quantum decoherence of near-surface nitrogen-vacancy centers in diamond and implications for nanoscale imaging*, Ph.D. thesis, University of California, Santa Barbara (2016).

[3] H. J. Mamin, M. H. Sherwood, M. Kim, C. T. Rettner, K. Ohno, D. D. Awschalom, and D. Rugar, Multipulse double-quantum magnetometry with near-surface nitrogen-vacancy centers, Phys. Rev. Lett. **113**, 030803 (2014).

[4] E. Bauch, C. A. Hart, J. M. Schloss, M. J. Turner, J. F. Barry, P. Kehayias, S. Singh, and R. L. Walsworth, Ultralong dephasing times in solid-state spin ensembles via quantum control, Phys. Rev. X **8**, 031025 (2018).

[5] J. F. Barry, J. M. Schloss, E. Bauch, M. J. Turner, C. A. Hart, L. M. Pham, and R. L. Walsworth, Sensitivity optimization for NV-diamond magnetometry, Rev. Mod. Phys. **92**, 015004 (2020).

[6] T. J. DiCiccio and B. Efron, Bootstrap confidence intervals, Stat. Sci. **11**, 189 (1996).

[7] S. Felton, A. M. Edmonds, M. E. Newton, P. M. Martineau, D. Fisher, D. J. Twitchen, and J. M. Baker, Hyperfine interaction in the ground state of the negatively charged nitrogen vacancy center in diamond, Phys. Rev. B **79**, 075203 (2009).